Research Article

Influence of Fe-rich phases and precipitates on the mechanical behaviour of Al-Cu-Mn-Fe-Sc-Zr alloys studied by synchrotron X-ray and neutron

Yuliang Zhao [a,b,*], Dongfu Song [c,d], Shengchuan Wu [e,*], Shunfu Xie [c,f], Haoliang Wang [a], Mengmeng Wang [g], Weiwen Zhang [c], Zhenzhong Sun [a], Yubin Ke [f,h], Shanfeng Wang [h], Wanxia Huang [h], Ricardo Fernández [b,*]

[a] Neutron Scattering Technical Engineering Research Centre, School of Mechanical Engineering, Dongguan University of Technology, Dongguan 523808, China
[b] Centro Nacional de Investigaciones Metalúrgicas (CENIM), C.S.I.C., Avda. de Gregorio del Amo 8, Madrid 28040, Spain
[c] National Engineering Research Centre of Near-Net-Shape Forming for Metallic Materials, South China University of Technology, Guangzhou 510641, China
[d] Institute of New Materials, Guangdong Academy of Science, Guangzhou 510650, China
[e] State Key Laboratory of Traction Power, Southwest Jiaotong University, Chengdu 610031, China
[f] Spallation Neutron Source Science Center, Dongguan 523803, China
[g] School of Materials Science and Engineering, Anhui Polytechnic University, Wuhu 241000, China
[h] Institute of High Energy Physics, Chinese Academy of Sciences, Beijing 100039, China

ARTICLE INFO

ABSTRACT

A multiscale methodology using scanning and transmission electron microscope, synchrotron X-ray nano-tomography and micro-tomography, small angle neutron scattering, and *in situ* synchrotron X-ray diffraction has been used, to reveal the effect of Fe-rich phases and precipitates on the mechanical behaviour of an Al-Cu-Mn-Fe-Sc-Zr alloy. The α-Al grains size is reduced from 185.1 μm (0 MPa) and 114.3 μm (75 MPa) by applied pressure. Moreover, it has been demonstrated that suitable heat treatments modify the 3D morphology of Fe-rich phases from interconnected to a disaggregated structure that improves the mechanical properties of the alloy. The size and morphology evolution of fine precipitates under different ageing temperature and time are revealed. At ageing temperature of 160 °C, the precipitates change from GP zones to θ' (around 75 nm in length) with ageing time increasing from 1 h to 24 h; the Vickers hardness increases from 72.0 HV to 110.7HV. The high ductility of the Sc, Zr modified Al-Cu alloy is related to the complex shape and the loss of interconnectivity of the Fe-rich particles due to the heat treatment. The evolution of the crystal lattice strains in α-Al, and β-Fe calculated during tensile test using *in-situ* synchrotron X-ray diffraction corroborates the influence of the microstructure in the ductility of the modified alloy.

© 2023 Published by Elsevier Ltd on behalf of The editorial office of Journal of Materials Science & Technology.
This is an open access article under the CC BY license (http://creativecommons.org/licenses/by/4.0/)

1. Introduction

Aluminium-copper (Al-Cu) based alloys are structural materials widely used in the transport and aerospace industries due to their outstanding high-specific strength, excellent corrosion resistance, and good elevated-temperature properties amongst light alloys [1–3]. As lots of these Al-Cu parts are coming to the end of their service lives, recycling and reuse of scraps has become the very productive route to reduce solid waste and save energy [4,5]. A common problem with recycled Al alloys is their high levels of Fe impurity, which forms hard and brittle Fe-rich phases during solidification [6]. These Fe-rich phases, especially plate-like or needle-like shapes, significantly reduce the elongation, fatigue strength, and tensile strength of alloys [7,8]. Hence, extensive attempts [9–11] have been made to modify the morphology of Fe-rich phases into less detrimental shapes. It is well known that up to 0.6% Mn (wt.%) combine with Fe to form complex-shaped and compact Fe-rich phases in Al-Cu alloys [7,9–11]. However, excess Mn content in these alloys results in the formation of an increased volume fraction of Fe-rich phases that decreases their tensile properties. Our previous studies also showed that Mn is an ideal element to reduce the formation of plate-like Fe-rich phases and enhance their properties [7]. However, it is necessary to improve the mechanical properties of Al alloys by reducing the size of plate-like Fe-rich

phases and Al grains. Manufacturing Al alloys by applying pressure during solidification is a useful method to refine microstructure and enhanced the mechanical properties [7,9–16]. Applying pressure above the liquids temperature force the liquid feeding and eliminate the formation of shrinkage and pores resulting in the improvement of mechanical properties, especially the ductility [7,9–11]. Also, applied pressure reduces the air gap between the solidifying metal and the metallic mould and thus increases their contact area and the heat-transfer coefficient [13]. This resulting higher cooling rate can also refine the size of Fe-rich phases and improve the properties [12–16].

This strategy can be combined with the addition of grain refiners in the alloy. Hereof, Scandium (Sc) is being recently added to Al-Cu alloys to improve grain refinement and mechanical properties [16–22]. The minor addition of grain refiner has a good grain refinement of Al alloys during solidification [23–31]. Previous studies [17–20] have systematically studied the effect of Sc addition to Al-Cu alloys, and found that Sc promotes the precipitation of θ'-Al_2Cu, reducing its size and narrowing the size distribution. It has also been reported that Sc addition can significantly reduce the grain size of the Al matrix, in which Al_3Sc serves as heterogeneous nucleation sites for α-Al [18]. Also, the number of θ'-Al_2Cu phases significantly increases with Sc addition, but their length and width clearly decrease [18]. Cu atoms segregate at the Al_3Sc/matrix interface, to form the Al_3Sc/θ'-Al_2Cu interface, which blocks the growth of Al_3Sc phases and increases the thermal stability of the Al_3Sc nanoprecipitates [19–21]. This similar phenomenon is also observed in the Al-Cu-Y, Al-Cu-Er, Al-Cu-Yb, and Al-Cu-Gd alloys [32,33]. However, the excess of Sc in Al-Cu alloys lead to the formation of the ternary intermetallic phase of W-Al_8Cu_4Sc, which consume the Cu solute available for precipitation, which decreases the mechanical properties [34,35]. In practice, Zr is combined with Sc added to Al-Cu alloys to refine the Al_3Sc precipitates and increase their thermal stability, finally resulting in the improved mechanical properties. [35–38]. These improvements are related to the presence of fine $Al_3(ScZr)$ precipitates that promote nucleation and refinement of the θ' precipitates during ageing.

The precipitation sequence of Al-Cu alloys is well established and can be summarized as follows [39,40]: supersaturated solid solution (SSSS)→Guinier Preston (GP) zone→θ'' precipitate→θ' precipitate→θ precipitate. However, grain refiners as Sc and Zr modify the precipitation kinetics. Small angle X-ray/neutron scattering (SAXS/SANS) is a powerful method providing rich information about the size distributions of precipitates in alloys [41–43]. Hence, SAXS and/or SANS are widely used to evaluate the size, shape and distribution of nano-precipitates in Al-Cu alloys during ageing [43]. The *in situ* SAXS method was used to study the real-time evolution of the thickness of θ' precipitates in Al-Cu alloys during non-isothermal heating [43]. However, the type and size of precipitates in Al-Cu-Mn-Fe-Sc-Zr under different ageing treatment are not clear yet.

Synchrotron radiation X-ray computed tomography (SRXCT) is a powerful technique that can determine the size, 3D morphology, and spatial distribution of intermetallic phases in Al alloys [44]. A number of investigations [45–48] have been carried out by the present authors to study the evolution of 3D morphology of Fe-rich phases in Al alloys using SRXCT. The Fe-rich phases in Al-Cu alloys have a complex interconnected network 3D structure [46–48]. Moreover, the *in situ* nano-scale SRXCT [49] has been used to capture the initiation and evolution of damage of 3D θ' precipitation in Al-Cu alloys during nanomechanical testing. The crack initiation and propagation processes in Al alloys during tensile and fatigue tests have also been studied by *in situ* SRXCT [50–57]. Crack initiation and propagation are most likely to occur at a hard eutectic Si, Fe-rich phase, and Al_2Cu phases in the vicinity of pores in A319 Al alloys [50]. The high Fe and Si contents in Al-Zn-Mg-

Cu form a high volume fraction of Fe-rich phases, which act as the initiation sites for the cracks during tensile tests and lead to a change from ductile to quasi-cleavage fracture [51]. Fe-rich phases and pores have an important role in strain distribution, crack propagation, and final fracture during the tensile test [52]. Cracks initiate at hard Fe-rich and eutectic Si phases around the pores in Al-Si-Cu alloys. These interconnected hard particles provide the route for crack propagation [53]. In recent years, the effect of secondary phases in the mechanical behaviour of light alloys is being extensively investigated during tensile tests using *in situ* High-energy Synchrotron Radiation X-ray Diffraction (SRXD) [58–62]. The combined study of the lattice strain and full width at half maximum (FWHM) allows describing how the secondary phases influence the mechanical properties of the alloy.

In this work, a comprehensive study has been carried out to describe the microstructural evolution in Al-Cu-Mn-Fe-Sc-Zr alloy during solidification and after T5 ageing treatment and their effect on the mechanical behaviour of the alloy. In particular, the influence of Fe-rich particles and precipitates that greatly influence mechanical behaviour has been clarified. Moreover, the influence of 3D morphology and distribution of Fe-rich on the strain in grains of the polycrystal during the tensile test has also been determined by micro-scale and nano-scale SRXCT and *in situ* SRXD.

2. Experimental procedure

2.1. Sample preparation

The studied alloys were prepared using commercial pure Al (99.9%) and, Al-50Cu, Al-10Mn, Al-10Fe, Al-2Sc, and Al-2Zr master alloys. In total, 5 kg of raw materials were melted in a graphite crucible inside an electric-resistance furnace. They were gradually heated to approximately 800 °C and then held at this temperature for 0.5 h for homogenization. 0.2% hexachlorobenzene (C_2Cl_6) was added into the Al melts for slag removal and degassing. Then, the Al melts were cooled to 750 °C and prepared for casting. Finally, the melts were poured into a steel mould (preheated to 250 °C). For the squeeze casting, the melt was solidified under 75 MPa applied pressure [9–11]. This applied pressure during solidification eliminates the pores and refines the microstructure. To study the evolution of the precipitates of the studied alloys, the resulting cast ingots were heated at 538 °C for 12 h to obtain a supersaturated solid solution. Samples from these ingots were subjected to heat treatments at 120 and 160 °C for 1, 4, 12, and 24 h, respectively, to study the influence of ageing on the mechanical properties of the alloys. Considering the relationship between ageing treatment and hardness in Al-Cu alloys, the typical heat treatment process was used: solid solution at 538 °C for 12 h and ageing 160 °C for 8 h. The chemical composition of the Al-Cu-Mn-Fe-Sc-Zr alloy was analysed by using an optical emission spectrometer as 4.91% Cu, 0.61% Mn, 0.30% Fe, 0.10% Sc, 0.08% Zr in weight.

2.2. 2D microstructural and mechanical characterization

Samples with 10 mm in diameter and 20 mm in height for metallographic observation were cut directly from the ingots. They were prepared through the standard metallographic process of grinding, polishing, and etching with 4% HNO_3 aqueous solution. The samples were observed using a scanning electron microscope (SEM, Zeiss Sigma 500, Germany) coupled with an energy-dispersive spectrometer (EDS, Oxford, UK). The operating voltage is 20 kV. The morphology of Fe-rich phases was determined by dissolving the α-Al matrix of the samples using a mixed solution of iodine and methanol (4–5 h). An X-ray diffractometer (XRD, Rigaku Smartlab, Japan) with a Cu target (diffraction angle: 0–90°, step: 0.013°) was used to study the different phases present in the

studied alloy. The morphology evolution of the precipitates was determined by TEM (Tecnai G2 F30) with EDS analysis, operated at 200 kV. The phase transformation temperature was determined by differential thermal analysis (DTA, NETSCH Jupiter STA 449 F3). These samples were heated with a heating rate of 10 °C/min into an argon atmosphere. The Electron Back-scatter Diffraction, EBSD samples were polished using a vibration-polishing machine (ZPG-300, China) for 4 h with a frequency of 58 Hz. The samples were tilted 70° with respect to the SEM detector and the sample to detector distance was 10 mm. The step size was 2 μm × 2 μm. The data were analysed using HKL Channel 5 software. The strength of the alloys under different ageing times was determined by Vickers micro-hardness. A load of 50 g was applied with a holding time of 10 s. At least 10 measurements were repeated to get the average value.

2.3. Ex-situ *synchrotron X-ray tomography experiment*

The micro-scale synchrotron X-ray tomography experiments were performed at BL13HB beamline, Shanghai Synchrotron Radiation Facility (SSRF), Shanghai, China. The detailed experimental description can be found elsewhere [45,63]. The samples for tomography experiments were machined into 1 mm diameter cylinders. The spatial resolution was 0.65 μm/pixel. The samples rotated 180° and 1200 projections were obtained during the rotation. The exposure time was 0.3 s for every single projection. These projections were reconstructed using PITRE and PITRE-BM software [64]. The 3D morphologies of Fe-rich phases and pores were extracted by Avizo software. The detailed reconstruction procedure can be found in the Refs. [45–48].

Due to the extremely complex morphology of the Fe-rich phases, it is very difficult to clearly describe the 3D morphology of Fe-rich phases with a pixel size of 0.65 μm. For this reason, two samples with heat-treatments were studied by nano-scale SRXCT. The nano-scale synchrotron X-ray tomography experiments were performed at 4W1A beamline, Beijing Synchrotron Radiation Facility (BSRF), Beijing, China. The detailed description of the nano-CT setup can be found in Ref. [65]. The energy of the full-field transmission X-ray microscopy is 8 keV. The detector is formed by an array of 1024 × 1024 pixels. The effective pixel size of the study is about 64 nm. The field of view is 65 μm × 65 μm. After the projections were collected, they were reconstructed by the software provided at the beamline station.

2.4. Small angle neutron scattering (SANS) experiment

SANS was used to measure the size and distribution of precipitates in the alloys under different ageing statement. SANS experiments were performed at the SANS beamline of China Spallation Neutron Source (CSNS), Dongguan, China. The power of the neutron source was 50 kW. The incident neutrons with a wavelength range from 1 Å to 9 Å were used. The sample to detector distance was 4 m and a sample aperture of 6 mm in diameter was used in the measurements. The detector array was composed by linear He-3 gas tubes, which cover the Q-range between 0.01 Å^{-1} and 0.6 Å^{-1}. The collection time for the scattering experiment was approximately 2 h for each sample. Neutron data were corrected for background scattering (empty sample holder), transmission and detector efficiency, and set to absolute units. The details of the correction process can be found in [66]. The size and distribution of the precipitates in the alloys were analysed by a combination of power-law + spheroid models. The fit process of the SANS data was carried out by using the Igor software [67]. The spheroid model considers two contributions to the SANS curves: (a) low-Q region corresponding to power law scattering from the boundary of large obstacles, such as coarse precipitates, and grain boundaries; (b) high-Q region corresponding to small precipitates. The total scattering intensity is therefore described by [68]:

$$I(Q) = AQ^m + N_\mathrm{p}(\Delta\rho)^2 \left(\frac{4}{3}\pi\right)^2 \int_0^\alpha F(R)R^6 P(QR)\mathrm{d}R + B_\mathrm{g} \tag{1}$$

where $I(Q)$ is the scattering intensity, $Q = 4\pi\sin\theta/\lambda$ is the momentum transfer modulus, A is a scale factor. The Porod-type contribution is described by the AQ^m power law m is the decay exponential coefficient. N_p is the number density of precipitates, $\Delta\rho$ is the difference in the neutron scattering length distance between the precipitates and the matrix.

2.5. In situ *synchrotron X-ray experiments*

The tensile test synchrotron X-ray tomography experiments were performed at BL13HB beamline, Shanghai Synchrotron Radiation Facility (SSRF), Shanghai, China [42–45]. This quasi-*in situ* X-ray tomography experiment was used to observe the damage evolution during the tensile test. The image height was 4 mm, and the pixel size was 3.25 μm. The photon energy was 26 keV and the exposure time was 0.5 s per projection. Projections were acquired every 0.25° within a range of 180° using a step-scan mode, giving 720 projections for volume reconstruction. The reconstruction and 3D rendering scheme for processing the projection images are the same as the one described in Section 2.3.

The *in situ* tensile and ageing test with synchrotron X-ray diffraction experiments were performed at BL14B1 beamline, Shanghai Synchrotron Radiation Facility (SSRF), Shanghai, China. The aim of *in situ* tensile test is to study the crystallographic orientation strains during the tensile test. It provides a beam energy of 18 keV, beam size = 200 × 200 μm^2, and a wavelength of $\lambda = 0.688$ Å. The detailed description of *in situ* tensile test set up in the beamline can be found in the Refs. [58,59]. The T5 heat-treated (solid-solutioned at 538 °C for 12 h, and ageing at 160 °C for 8 h) samples with a size of 40 mm × 2 mm × 0.8 mm were used for the *in situ* tensile test. During *in situ* test, the sample was positioned in perpendicular to the X-ray path. The constant strain rate during the test was 5 × 10^{-4} s^{-1}. The 34 diffraction patterns were recorded by a 2D detector, for which the axial direction was parallel to the tensile axis. The 2D diffraction patterns were analysed with the Fit2D software. The lattice strain can be obtained from the peak shifts, as shown below [58,60]:

$$\varepsilon_{hkl} = \frac{d^{hkl} - d_0^{hkl}}{d_0^{hkl}} \tag{2}$$

where d_0^{hkl} and d^{hkl} are the stress-free and stress d-spacing for the (hkl) plane, respectively.

The *in situ* synchrotron X-ray diffraction experiment during ageing treatment was used to study the early stage of precipitation of θ'. The heating setup used was the Linkam (UK) system with a water-cooling system. The temperatures during ageing were calibrated using RbNO$_3$ powders. The sample was heated from 29 °C to 160 °C with a constant heating rate of 5 °C/min (23 diffraction patterns, every minute take one pattern), then held at 160 °C for 4 h (15 diffraction patterns, every 15 min take one pattern).

3. Results

3.1. As-cast and heat-treated microstructures

Fig. 1 shows the typical SEM images for both as-cast and heat-treated (solid-solution at 538 °C for 12 h + ageing at 160 °C for 8 h) alloys solidified without and with applied pressure. As shown in Fig. 1(a) and (c), the eutectic intermetallic phases changed from elongated morphologies to refined and separated
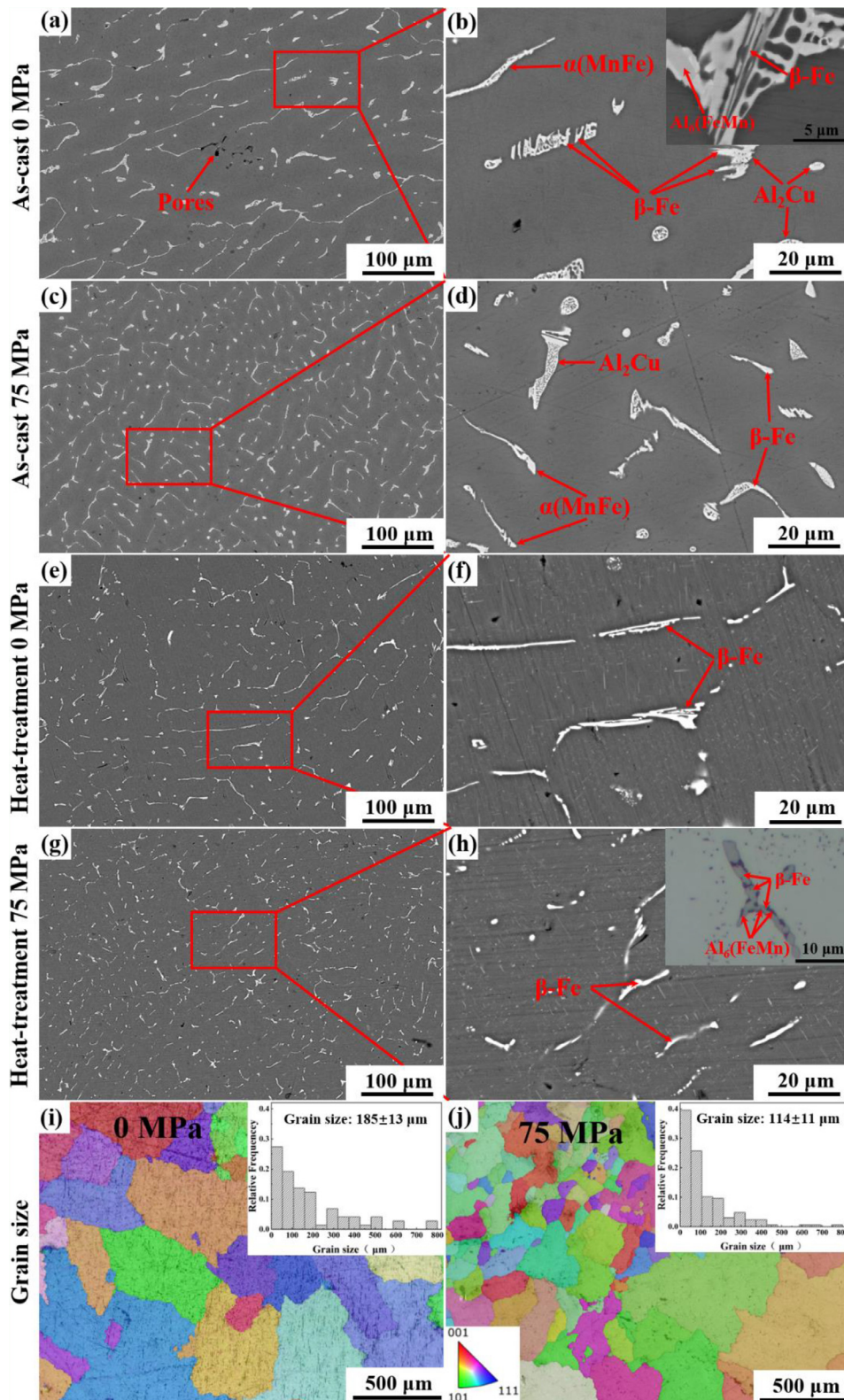
Fig. 1. Intermetallic phases in: (a–d) as-cast state; (e–h) heat-treated state (solid-solution + ageing at 160 °C for 8 h); (a, b, e, f) 0 MPa during solidification; (c, d, g, h) 75 MPa during solidification; the EBSD maps and grain size distribution of the heat-treated alloys: (i) 0 MPa and (j) 75 MPa.

morphologies by applying pressure. The inserted image in Fig. 1(b)) shows that the grey $Al_6(FeMn)$ phases, plate-like β-Al_7Cu_2Fe (β-Fe) phases and white Al_2Cu phases coexist. It is also found that the pores are mostly eliminated when the alloys are solidified under pressure at 75 MPa. The 0 MPa as-cast alloys show sev-

eral intermetallic phases, α-$Al_{15}(FeMn)_3Cu_2$ (α(MnFe)), β-Al_7Cu_2Fe (β-Fe), $Al_6(FeMn)$ and Al_2Cu phases, as indicated by Fig. 1(b) and (d). During solid-solution treatment, the Al_2Cu phases are dissolved into the Fe-rich phases and the Al matrix, Fig. 1(e) and (g). Cu atoms diffuse into α(MnFe) and β-Fe (as-cast state)
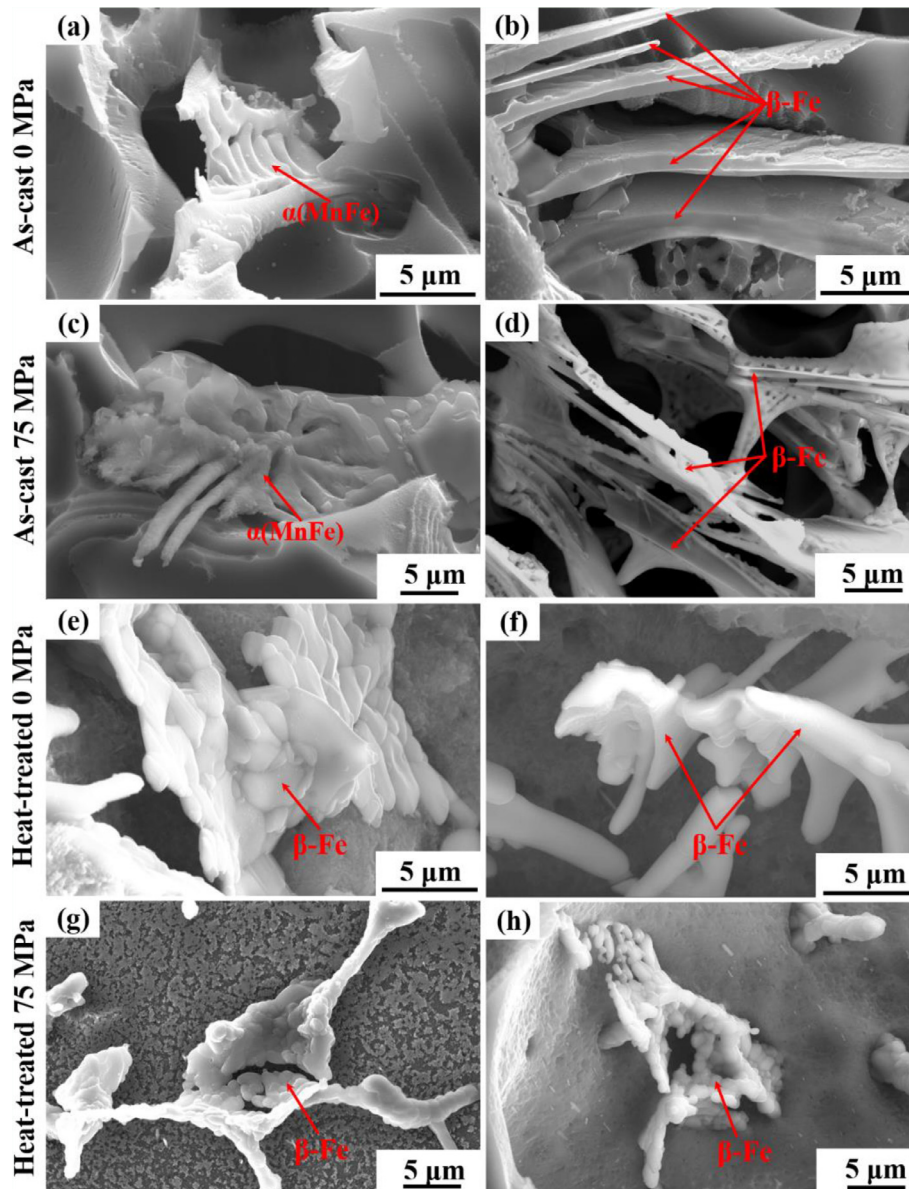
Fig. 2. Fe-rich intermetallic 3D morphology in: (a–d) as-cast state; (e–h) T5 heat-treated state; (a, b, e, f) 0 MPa; (c, d, g, h) 75 MPa.

and form the heat-treated β-Fe (Al$_7$Cu$_2$Fe). In the as-cast state, the β-Fe phases are formed through the coupled eutectic reaction: L→ β-Fe + Al$_2$Cu + Al. In the heat-treated state, the β-Fe phases are formed through the solid-state transformation α(MnFe)/Al$_6$(FeMn) + Al$_2$Cu→ β-Fe + Al. The Fe-rich phases are fragmented into spherical particles after heat treatment (see Fig. 1(f) and (h)). The inserted OM image in Fig. 1(h) shows that the grey β-Fe and purple Al$_6$(FeMn) phases coexist in the heat-treated alloys. Furthermore, the mean size of β-Fe in the alloy with 75 MPa applied pressure is slightly smaller than in those of the alloy without applied pressure. The type of Fe-rich phases is examined by SEM-EDS, the results are listed in Table 1. The EBSD images and the size distribution of the heat-treated alloys without and with 75 MPa applied pressure are presented in Fig. 1(i) and (j). The grain size for the two alloys investigated is 185±13 μm (0 MPa) and 114±11 μm (75 MPa), respectively. This indicates that the application of pressure is beneficial to refine the grain size of the studied alloys. The application of pressure reduces the air gap between the solidifying metal and the metallic mould and

Table 1
The alloy composition of intermetallic phases in the studied alloys (at.%).

State	Phases	Mn	Fe	Cu	Si	Al
As-cast	α(MnFe)	2.2	5.09	6.3	0.8	Balance
	β-Fe	1.3	4.5	13.5	–	Balance
	Al$_6$(FeMn)	3.6	12.9	1.0	–	Balance
Heat-treated	β-Fe	1.8	6.0	15.6	–	Balance
	Al$_6$(FeMn)	0.9	9.4	9.4	–	Balance

thus increases the contact area; effecting improvement in the heat-transfer coefficient, resulting in the increase of a higher cooling rate.

Fig. 2 illustrates the 3D morphology of Fe-rich phases under different conditions, revealed by removing the Al matrix, using deep-etched methods. The Chinese-script α(MnFe) and plate-like β-Fe presented in the as-cast samples are shown in Fig. 2(a)–(d). These Fe-rich phases are formed at the late solidification stage

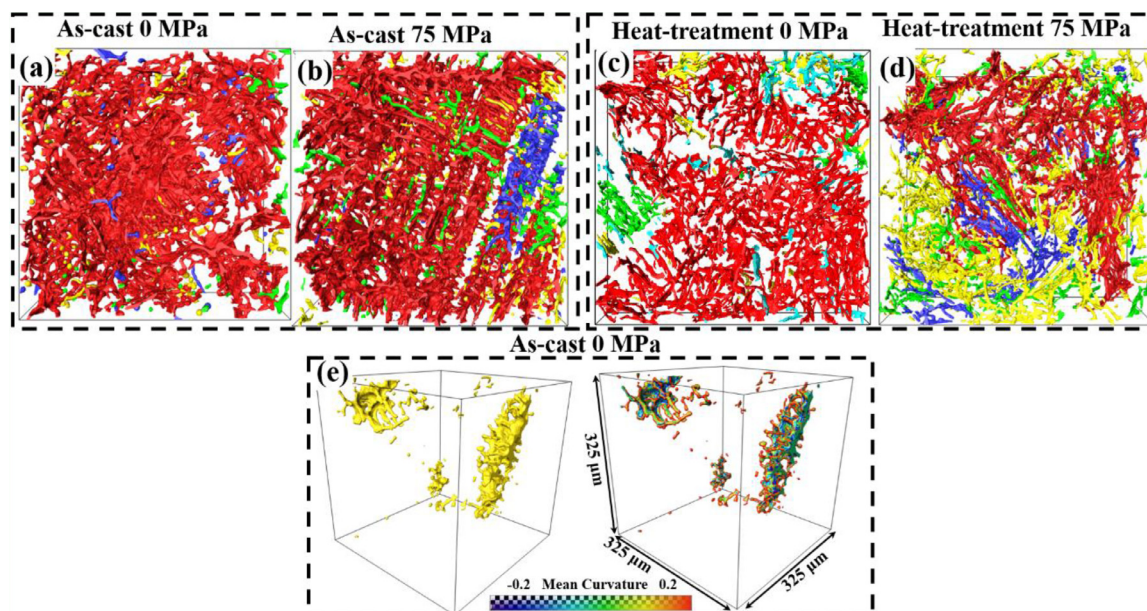**Fig. 3.** Effect of the applied pressure during solidification on the 3D morphology of Fe-rich phases: (a, b) as-cast Fe-rich phases and Al$_2$Cu (c, d) heat-treated Fe-rich phases; (e) pores in as-cast alloys.

through the coupled eutectic reaction [7]. It is found a reduction in the thickness of the β-Fe particles in the alloy with applied pressure during solidification (Fig. 2(b) and (d)). After the T5 heat treatment, the 3D morphology of Fe-rich phases in the alloys undergo spheroidized; *i.e.,* they are composed of interconnected small bumps and holes (see Fig. 2(e)–(h)). The deep-etched images, Fig. 2(a)–(d), clearly show the rough surface of Fe-rich intermetallic phases. This rough surface of the Fe-rich intermetallic is a clear indication of a solid-state transformation as this phase shows a flat surface in the as-cast state. The small holes correspond to the Al spots dissolved by deep-etched, as shown in Fig. 2(g) and (h).

3.2. 3D morphology of Fe-rich phases and pores

The 3D morphology of Fe-rich phases and pores present in the alloys under different solidification and heat treatment conditions are shown in Fig. 3. It can be seen in Fig. 3(a, b) that some Fe-rich particles are interconnected in 3D space (indicated by red colour). The interconnection of particles cannot be distinguished in the 2D metallographic observations. These interconnected particles are formed through the coupled eutectic reaction at the late solidification stages. Moreover, it has been found that Fe-rich phases are also developed in the interdendritic regions, Fig. 3(b). It is found that the volume fraction of separated Fe-rich particles in the alloy with applied pressure, Fig. 3(b) is higher than those of the alloys solidified without applied pressure, Fig. 3(a). Similarly, the volume fraction of separated Fe-rich particles (Fig. 3(c) and (d)) is also higher, this meaning that heat treatment can break the interconnectivity of Fe-rich particles during solid-state transformation. Fig. 3(e, f) shows the 3D morphology of pores in the alloys. Two large shrinkage pores (length range from 100 μm to 300 μm) and small hydrogen pores are observed in Fig. 3(e). The shrinkage pores are formed in the interdendritic regions, due to the lack of liquid feeding; while gas pores are the results of hydrogen gas entrapment during solidification due to the decreasement in solubility. The size of the pores in the alloy solidified under 75 MPa applied pressure is below the detection limit. So, we assume that the pores in this alloy are eliminated.

Despite the relatively good pixel size (0.65 μm) of microtomography, it is difficult to observe the 3D eutectic morphology

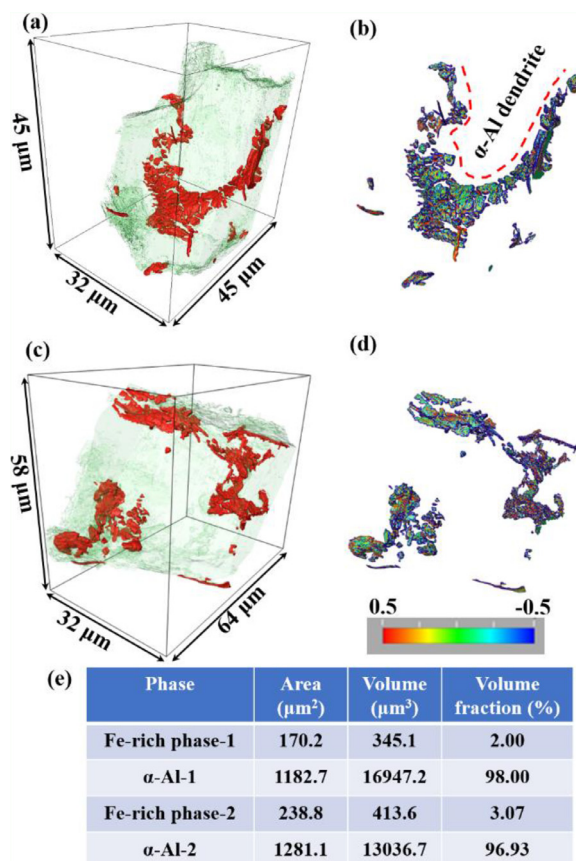| Phase	Area (µm²)	Volume (µm³)	Volume fraction (%)
Fe-rich phase-1	170.2	345.1	2.00
α-Al-1	1182.7	16947.2	98.00
Fe-rich phase-2	238.8	413.6	3.07
α-Al-2	1281.1	13036.7	96.93

Fig. 4. (a, c) 3D morphology and (b, d) mean curvature of Fe-rich phases in T5 heat-treated 75 MPa alloys reconstructed by nano-tomography; (e) statistical analysis.

of the Fe-rich phases in detail. Thus, a nano-tomography method (pixel size about 100 nm) in 4W1A beamline in BRSF was used to study the high-resolution morphology of the Fe-rich phases in the heat-treated at 75 MPa alloy, Fig. 4. Fig. 4(a) indicates that
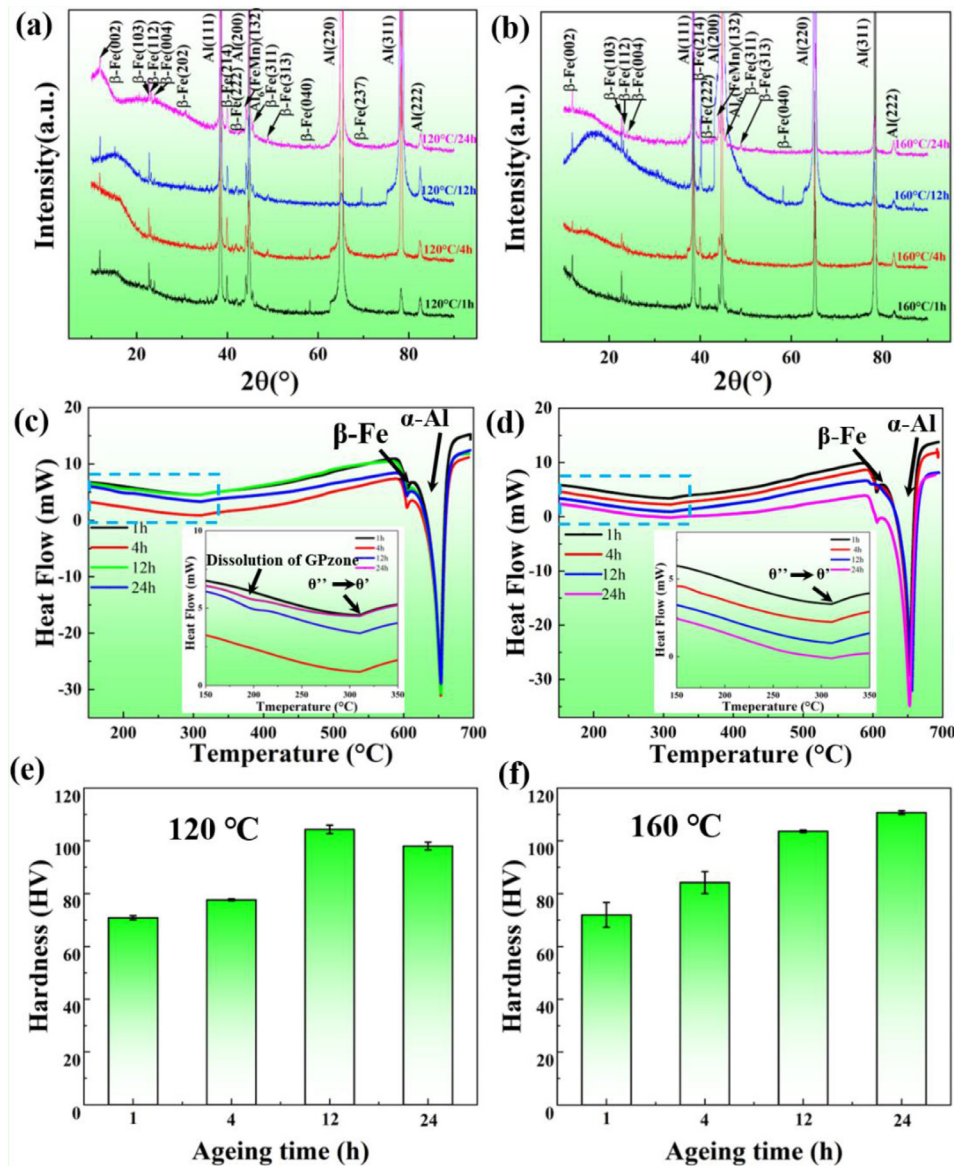
Fig. 5. X-ray diffraction patterns of the 75 MPa alloy after quenched at different ageing temperatures of 120 °C (a) and 160 °C (b); DSC curve at different ageing temperatures of 120 °C (c) and 160 °C (d); the Vickers hardness of the Al matrix at different ageing temperatures at 120 °C (e) and 160 °C (f).

the Fe-rich particles are composed of several small and interconnected particles, which is consistent with the deep-etched images, (Fig. 2(e)–(h)). The concave spatial structure is formed in the narrow space between interdentric regions. Also, high-resolution 3D images, Fig. 4(a) and (c) and their mean curvatures, Fig. 4(b) and (d) further confirm that the surface of Fe-rich phases changes from flat in the as-cast state, to rough and separated after the T5 heat-treatment. The area and volume fraction of the Fe-rich phase in T5 heat treatment two samples are 170.2 μm^2 and 238.8 μm^2; 2.00% and 3.07%, respectively.

3.3. Microstructural evolution during ageing treatment

The effect of the ageing treatments (described in Section 2.1) on the microstructure of studied alloys has been studied. Fig. 5 illustrates the microstructure evolution of the alloys with the heat treatments described in Section 2.1 characterized by XRD, DSC, and Vickers hardness. As shown in Fig. 5(a) and (b), the microstructure of the studied alloys consists of α-Al, β-Fe and Al$_6$(FeMn) phases at different ageing temperatures. The α(MnFe) phases in the as-

cast state are completely converted into β-Fe in the heat-treated alloy. This indicates that the ageing processes do not change the composition of the main phases. Fig. 5(c) and (d) show the DSC curves of the studied alloys with different ageing temperatures and times. There are three main endothermic peaks in the alloys, which correspond to the transformation of θ'' to θ' (near 300 °C), melt of β-Fe (about 600 °C), and Al (approximately 660 °C). In addition, it can be seen from Fig. 5(c) that there is a weak endothermic peak at 150–200 °C related to the dissolution of GP zones. This means that the formation of a GP zone needs a long ageing time at a temperature of 120 °C. The Vickers hardness of the alloys with different ageing temperatures and time are presented in Fig. 5(e) and 6(f). At ageing temperatures of 120 °C the hardness first increases from 71±1 HV at 1 h to 104±2 HV at 12 h and then decreases to 98±2 HV at 24 h. At the ageing time of 160 °C, the hardness increases from 72±5 HV at 1 h to 111±1 HV at 24 h.

Fig. 6 shows the small angle neutron scattering (SANS) curves for the studied alloys under different heat treatment times and temperatures. As shown in Fig. 6(a) at 120 °C ageing temperature, the *I(Q)* show a linear part at the low Q zone (contribution from
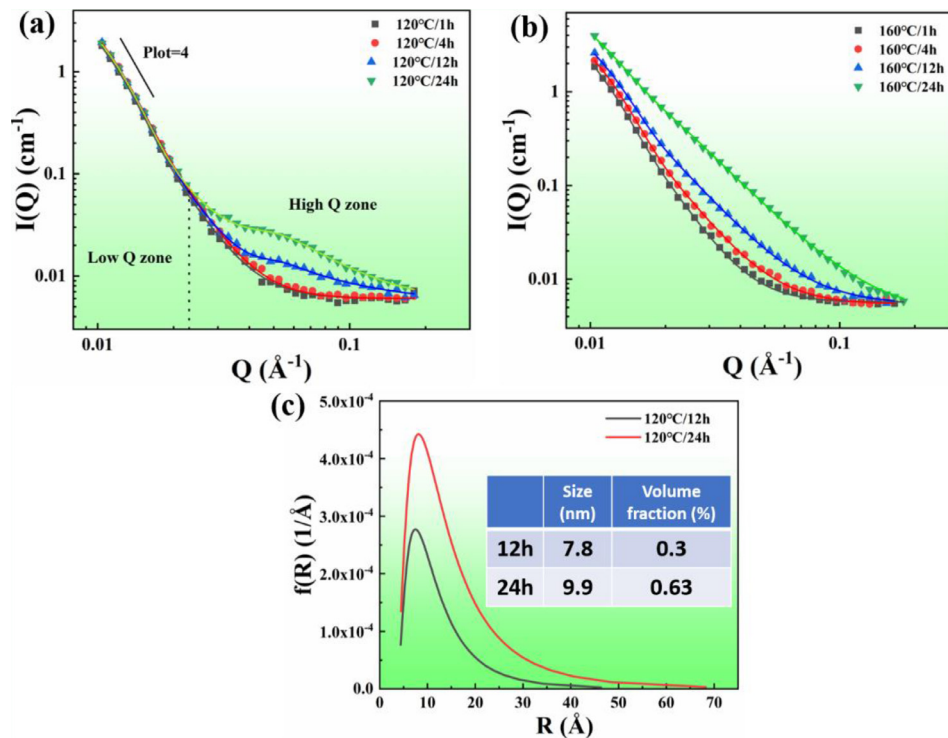
Fig. 6. SANS curves of the studied alloys at different ageing times: (a) at 120 °C and (b) at 160 °C; (c) size distribution of the precipitates at 120 °C ageing temperature for 12 and 24 h.

the large intermetallic phases, precipitates and background) and a curved part at the high Q zone (contribution from fine precipitates). As the ageing time increases from 1 h to 24 h at 120 °C, $I(Q)$ increases in the high Q zone indicating an increase in the volume fraction of fine precipitates. Fig. 6(c) shows the corresponding size distribution of the precipitates in the samples after 12 and 24 h at 120 °C. The equivalent diameter and volume fraction of precipitates vary from 7.8 nm and 0.3% at 12 h to 9.9 nm and 0.63% at 24 h. As shown in Fig. 6(b), the profiles of samples subjected to ageing at 160 °C for different times, has a straight line, indicating that the fine precipitates population continually grows. Due to the size of precipitates exceeding the CSNS measurement range, the size and volume fraction of precipitates at 160 °C are not considered in this work.

Fig. 7 shows the precipitates present in the Al-Cu-Mn-Fe-Sc-Zr alloys subjected to different ageing treatments. As shown in Fig. 7(a)–(h), the rod-like $Al_{20}Cu_2Mn_3$ (T) phases are randomly distributed in the Al matrix. The size of T phases is relatively stable at low ageing temperatures. A higher number density of precipitates is found in the vicinity of T phases with longer ageing times, as shown in Fig. 7(f)–(h). Thus, high magnification of TEM micrographs shows the distribution and evolution of fine precipitates, as shown in Fig. 7(i)–(p). The selected area diffraction patterns (SADPs) view along $[0\bar{1}1]$ or $[01\bar{1}]$ or $[\bar{1}10]$ zone axis of Al matrix is shown in Fig. 7. The high-resolution TEM (HRTEM) images of the precipitates (GP zones, θ'' and θ' phases) are shown in the inserted images of Fig. 7(i)–(p). At 120 °C and 160 °C, the length of the precipitates gradually increases with ageing time, this phenomenon is especially noticeable at 160 °C-12 h and 24 h, Fig. 7(o)–(p). The θ' phases are usually nucleated in the $Al_3(ScZr)$ precipitates (see Fig. 7(o)–(p)). TEM dark field micrographs were used to characterize the $Al_3(ScZr)$ precipitates in the alloys during homogenous heating. A large number of round and fine precipitates are distributed in the Al matrix. The SADPs view along $[1\bar{1}0]$ zone axis of $Al_3(ScZr)$ precipitates, Fig. 8. Some of them are

randomly distributed in Al matrix (Fig. 8(a), (c)–(e)), while others form a long necklace composed of several fine precipitates (Fig. 8(b), (f)–(h)). It is very usual to find grain boundaries decorated by $Al_3(ScZr)$ precipitates forming a necklace chain both at 120 °C and 160 °C, due to the grain boundary pipe diffusion [69].

The size and aspect ratio of GP zones, θ'', and θ' precipitates with different ageing times and temperatures are summarized in Fig. 9. It can be seen from Fig. 9(a) that the length and width of GP zones, θ'', and θ' precipitates at 120 °C increased from 0.9 nm and 0.4 nm to 3 nm and 13 nm, respectively. The size of θ' precipitates at the ageing temperature of 160 °C at 24 h grows into a large size (about 75 nm in length). Also, their aspect ratio increases with the ageing time (Fig. 9(b)).

3.4. Lattice strains during tensile test studied by synchrotron X-ray

The evolution of lattice strain in different crystallographic planes of different phases is helpful to understand the deformation mechanism. *In situ* synchrotron X-ray diffraction was used during the tensile test of 75 MPa alloy, to describe the influence of the microstructure in the deformation behaviour of the alloy in T5 condition (solid-solution at 538 °C for 12 h + ageing at 160 °C for 8 h) was used for the tensile test. Fig. 10(a) shows the 3D diffraction pattern in the strain range between 0 and 22.4%, in which α-Al (ICSD #43,423), β-Fe (ICSD #57,667), Al_6(FeMn) (ICSD #150,550), and θ'' (ICSD #151,384) peaks are identified. Due to the relatively low intensity of fine precipitate peaks in the studied alloy, the lattice strains were not analysed. Fig. 10(b)–(e) shows the evolution of 2D diffraction spectra with engineering strain of (111) and (022) planes in α-Al, (004) and (222) planes in β-Fe, (112) planes in Al_6(FeMn) and (010) in θ''. Fig. 11(a) shows the lattice strain *vs* engineering strains of (111) and (022) planes in α-Al and (004), (103), (214), (139), and (222) planes in β-Fe along the axial direction. Fig. 11(b) shows the evolution of the FWHM *vs.* engineering strains of β-Fe and α-Al. These planes have been selected for the
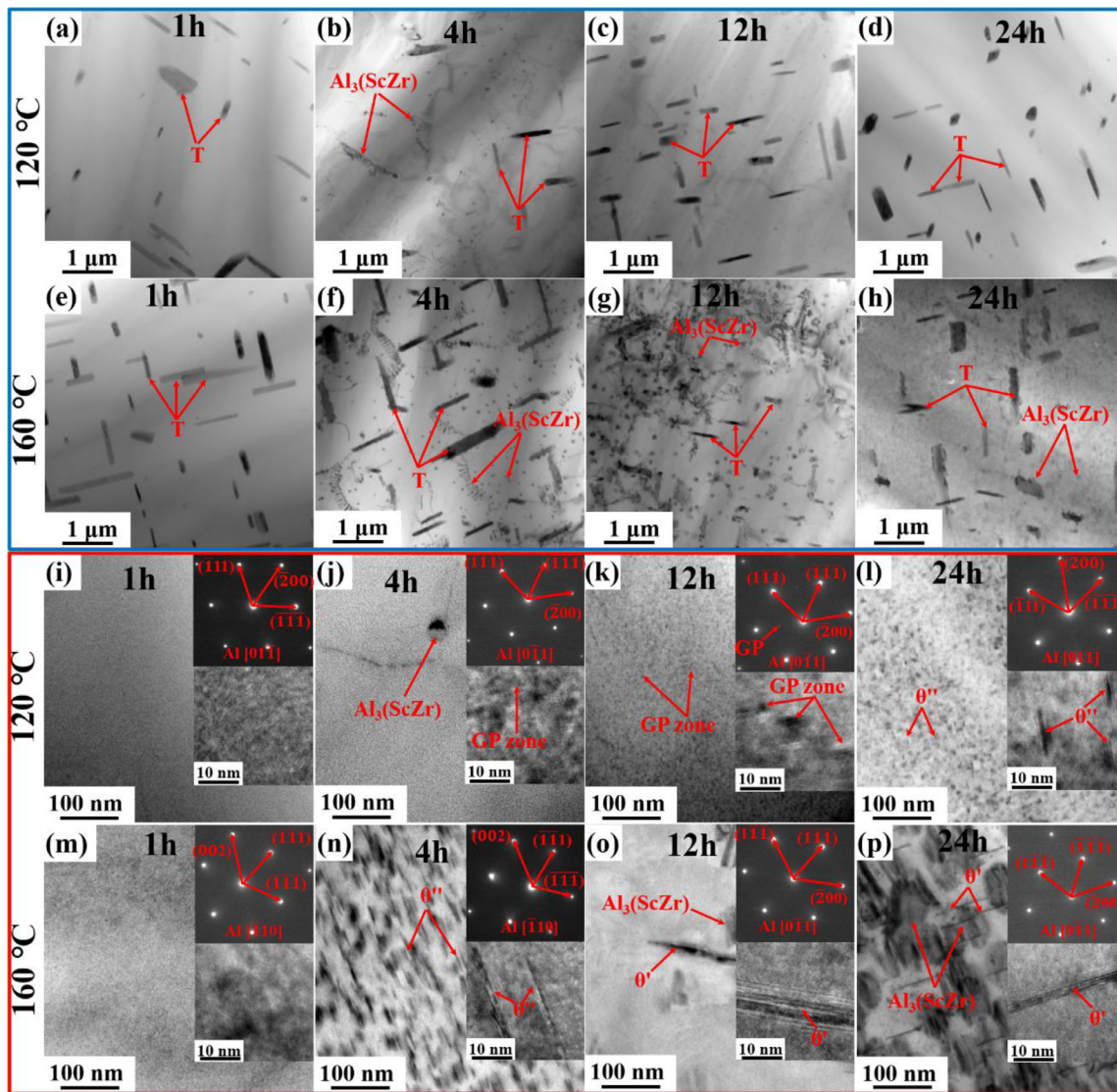
Fig. 7. TEM bright field micrographs, inserting HRTEM images and SADPs of 75 MPa alloys, showing T, GP zones, θ'' and θ' phases, and Al$_3$(ScZr) precipitates: (a, i) 120 °C 1 h; (b, j) 120 °C 4 h; (c, k) 120 °C 12 h; (d, l) 120 °C 24 h; (e, m) 160 °C 1 h; (f, n) 160 °C 4 h; (g, o) 160 °C 12 h; (h, p) 160 °C 24 h; (a–h) low magnification; (i–p) high magnification.

analysis because they show enough intensity and do not overlap with other phases. A Gaussian fitting was used for the analysis of the diffraction peaks. The lattice strain in the axial direction of the sample is obtained from Eq. (3). Since no d_0 is available, it is assumed that its initial value is the d_0^{hkl} at 0% strain. As shown in Fig. 11(a), at stage 1 (below 8% strain), the lattice strain linearly increases both for β-Fe and aluminium matrix. At stage 2, the lattice strain remains stable with increasing engineering strain in β-Fe (222) and β-Fe (004); while slightly decreases in β-Fe (214) and β-Fe (103) plane. The grains (111) and (022) of the Al matrix maintain a linear behaviour up to about 8% and 12% deformation, respectively. From that point, a steady state is reached. The different lattice strains obtained for every grain family, Fig. 11(b), can be explained by their elastic modulus and the presence of type II residual stresses [70]. Then the curvature in the lattice stain reflects the plastic behaviour of the matrix. However, the β-Fe phase shows no evolution of the lattice strain despite the increase in the engineering stress during the tensile test. At the near-fracture stage, the strain gradually concentrates which generates sample necking and final fracture around 22% of engineering strain (Fig. 11(a)). Fig. 11(c) shows the room temperature tensile behaviour of the so-

lidified alloy with an applied stress of 75 MPa heat-treated alloy. The yield strength of the alloy is 125 MPa. In the plastic regime, a hardening of about 80 MPa occurs and a total deformation of 22.4% (plastic deformation of 16%) is reached.

3.5. Damage evolution during tensile test studied by quasi-in-situ synchrotron X-ray tomography

The evolution of volume rendered pores and cracks in 0 MPa alloys during the tensile test at 0, 100, 120, 150, and 185 N are shown in Fig. 12. Before the tensile test, Fig. 12(a), shrinkage pores (around 1 mm) and fine hydrogen pores (approximately 10 μm) are homogeneously distributed in the alloy. These pores are formed directly during melt solidification [47]. As shown in Fig. 12(a$_2$)–(a$_5$), shrinkage pores are preferential sites for crack propagation (as shown by the red dashed line in Fig. 12(a$_4$)). The evolution of the mean curvature of pores with strain is shown in Fig. 12(a) and they are not significantly different. The mean curvature of shrinkage pores is 0; i.e., flat, and it is maintained constant with strain Fig. 12(a). The evolution of enlarged irregular hydrogen pores is shown in Fig. 12(b) and (c). It can be concluded that despite these
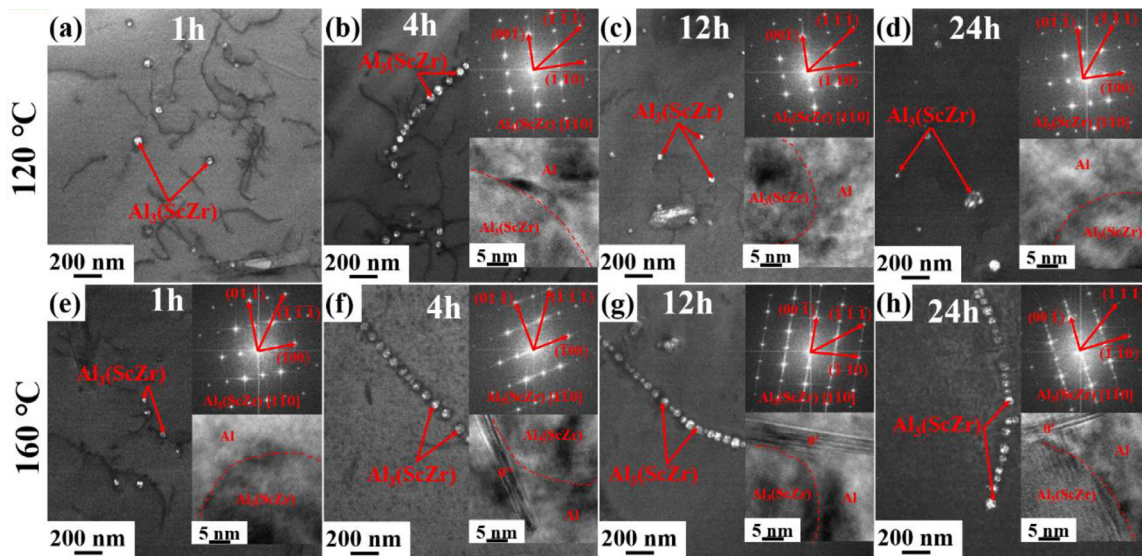
Fig. 8. TEM dark field micrographs, inserting HRTEM images and SADPs of 75 MPa alloys showing Al$_3$(ScZr) precipitates: (a) 120 °C 1 h; (b) 120 °C 4 h; (c) 120 °C 12 h; (d) 120 °C 24 h; (e) 160 °C 1 h; (f) 160 °C 4 h; (g) 160 °C 12 h; (h) 160 °C 24 h.
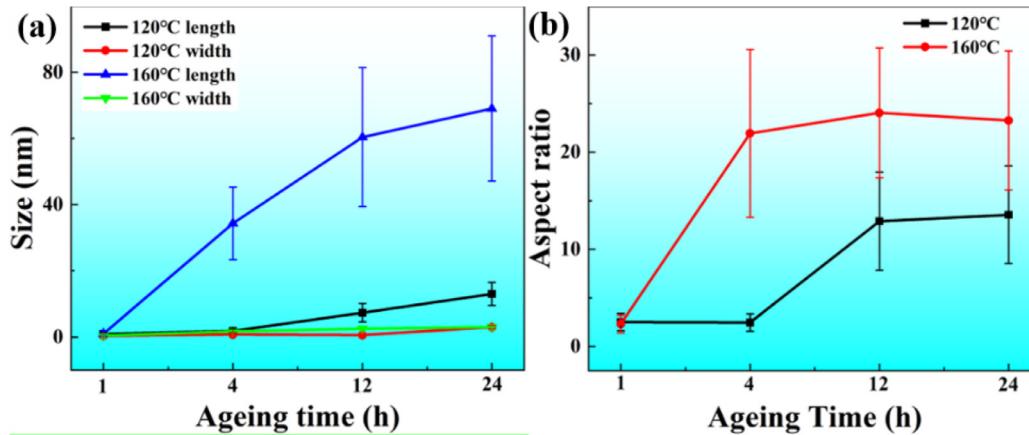

Fig. 9. Size and aspect ratio of the precipitates shown in Figs. 7 and 8: (a, b) GP zones, θ'' and θ' precipitates.

hydrogen pores expand during the tensile test, they do not contribute to the final failure due to their small size (in comparison to the shrinkage ones). The fracture surfaces of *in situ* sample are used to further understand the fracture process (Fig. 13). It can be seen that despite the high ductility of the alloy, the shrinkage pores and tear ridges are present in the fracture surface (Fig. 13(a)). As indicated by the 3D fracture surface (Fig. 13(b)), pores and cracks exist on the surface. The fractography in Fig. 13(c) and (d) shows the presence of dimples and a tear ridge, which indicates a small quantity of quasi-cleavage fracture.

4. Discussion

4.1. Solidification behaviour

The Al-Cu-Mn-Fe-Sc-Zr alloy is a typical coupled eutectic alloy according to Refs. [10,11]. The possible solidification sequence of the alloy is: (1) L→Al$_3$(ScZr); (2) L→Al$_3$(ScZr) + α-Al; (3) L→α-Al+ Al$_6$(MnFe); (4) L+ Al$_6$(MnFe)→ α-Al+ α(MnFe); (5) L→ α-Al+ Al$_2$Cu+ β-Fe. Thus, Chinese-script α(MnFe) phases are formed through the peritectic reaction, Fig. 2(a) and (c); while β-Fe phases are formed through the coupled eutectic reaction, Fig. 2(b) and (d). The size of the Fe-rich phases is smaller than in conventional alloys. This refinement of the Fe-rich phases is due to the high

cooling rate obtained by the applied pressure. The application of pressure reduces the air gap between the solidifying metal and the metallic mould and thus increases the contact area; effecting improvement in the heat-transfer coefficient, resulting in the increase of a higher cooling rate [13]. Apart from that, the Sc-rich phase has been located at the centre of Fe-rich phases, which indicates that Sc atoms are pushed into solute-rich interdendritic regions [71] due to their high thermal stability. Hence, they serve as heterogeneous nucleation sites for α(MnFe).

4.2. Precipitation kinetics

The fine precipitates are forming from the supersaturated Al matrix during the ageing process. As shown in the TEM images (Figs. 7 and 8) and their size statistics, the sizes of T phase and Al$_3$(ScZr) precipitates are relatively stable due to their thermal stability at ageing temperatures of 120 and 160 °C. Hence, only the θ'' or θ' coarsening kinetics during ageing is studied in the present work. The precipitation kinetics of θ'' or θ' precipitates in Al-Cu-Mn-Fe-Sc-Zr alloys can be described by the Liftshitz-Slyozov-Wagner (LSW) theory [72,73] for spherical precipitates. A generalization of this model for elliptical particles has been recently developed by Ref. [74]. In this general case:

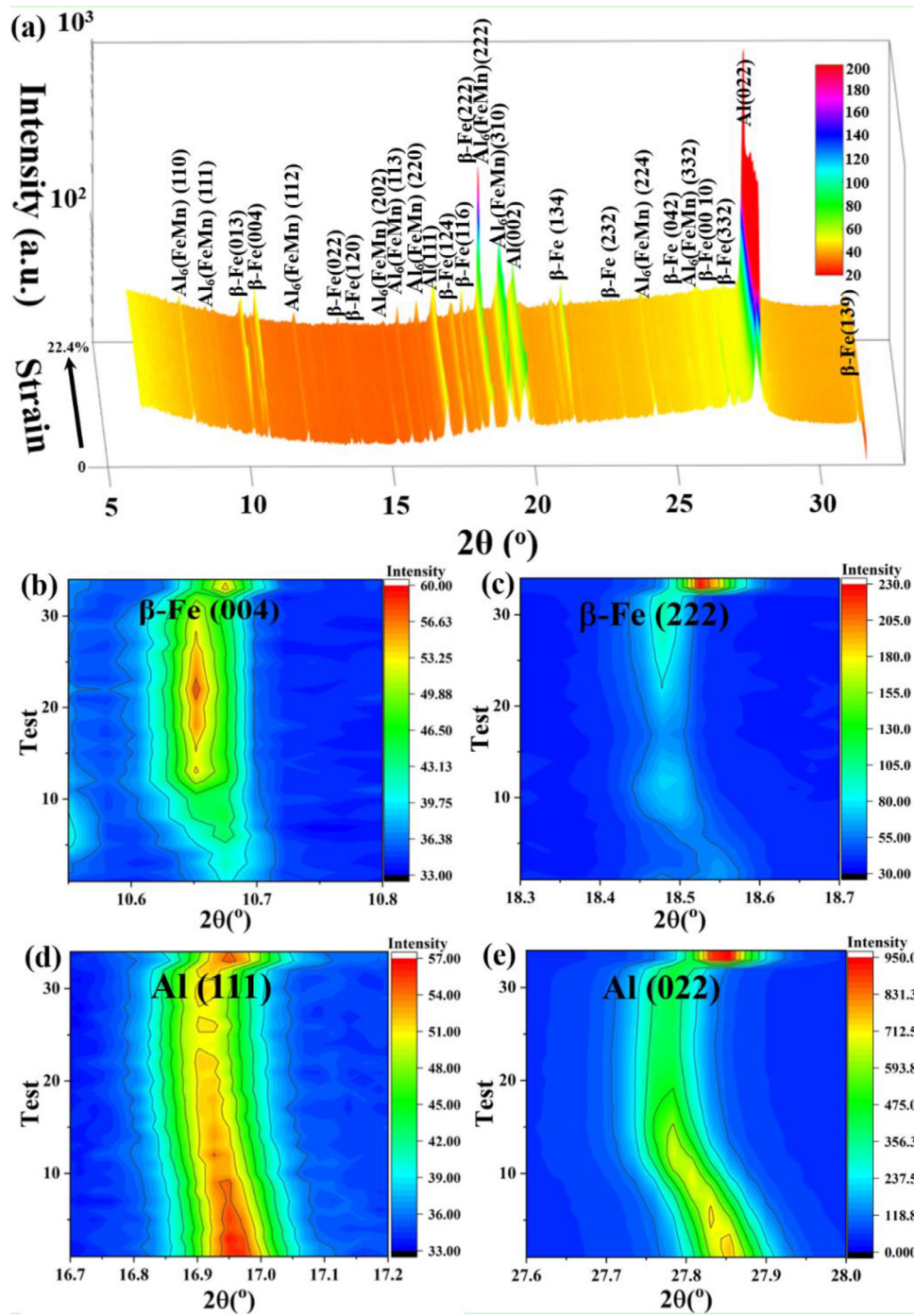$$d_2^n - d_1^n = K \cdot (t_2 - t_1) \tag{3}$$

Fig. 10. (a) *In situ* synchrotron X-ray diffraction patterns of 75 MPa alloys during tensile test; (b–e) enlarged view of the selected areas about the peak evolution of α-Al, and β-Fe with engineering strain.

where d_1 and d_2 are the average precipitates diameter (length in the TEM images) at the times t_1 and t_2, respectively; n is a parameter related to the geometry of the precipitates $1 < n < 3$ and K is the rate constant that depends on the temperature in the Arrhenius relationship. The rate constant K is related to the activation energy Q, depending on the temperature in an Arrhenius, and it [72] can be written as:

$$K = \frac{\kappa}{RT} \exp\left(\frac{-Q}{RT}\right) \tag{4}$$

where κ is a constant, R is the gas constant (8.314 J/(mol K)), T is the absolute ageing temperature and Q is the activation energy for

θ' precipitate growth. Hence, the calculation of Q can be obtained using the following equation [72]:

$$\ln(K \cdot T_a) = \ln\frac{\kappa}{R} - Q \cdot \ln\left(\frac{1}{RT_a}\right) \tag{5}$$

The plot of $R\ln(K \cdot T_a)$ *vs.* $1000/T_a$ gives a straight line whose slope gives the coarsening Fig. 14.

According to Eq. (2), d *versus* t has been plotted in Fig. 14(a). It is clearly seen a good linear fitting, with an exponent close to 1.6, for precipitation evolution at 120 °C and 160 °C, revealing that the LSW coarsening model is the dominant coarsening mechanism in θ' precipitates at 120 °C to 160 °C for the studied alloys. The
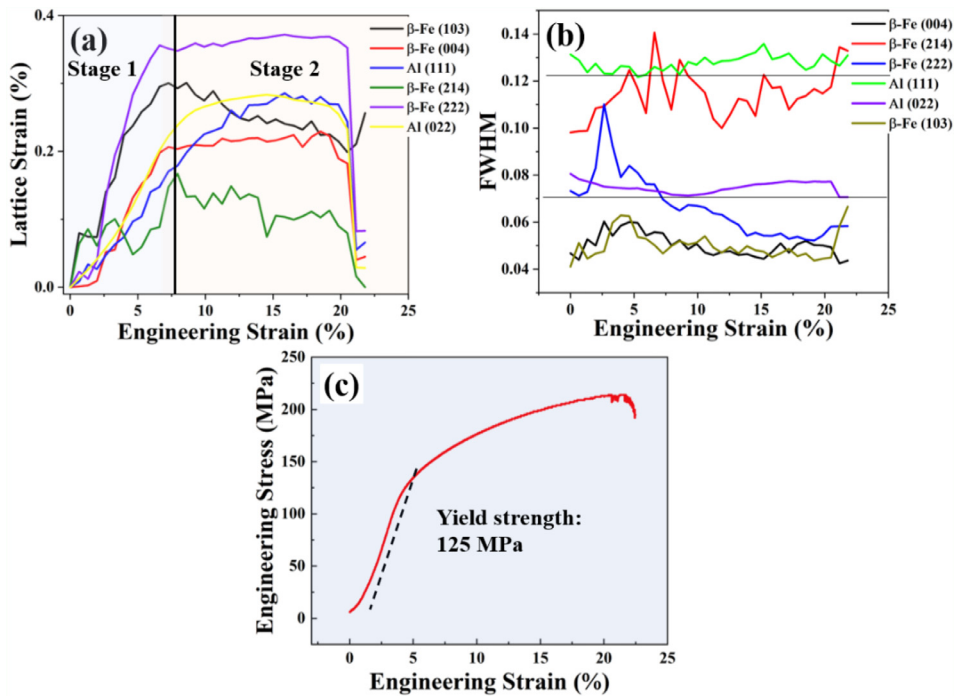
Fig. 11. (a) The lattice strain evolution of Al matrix and β-Fe phases as a function of engineering strain along the axial direction; (b) the FWHM evolution of Al matrix and β-Fe phases as a function of engineering strain; (c) engineering stress *vs.* engineering strain of the 75 MPa alloy at room temperature.
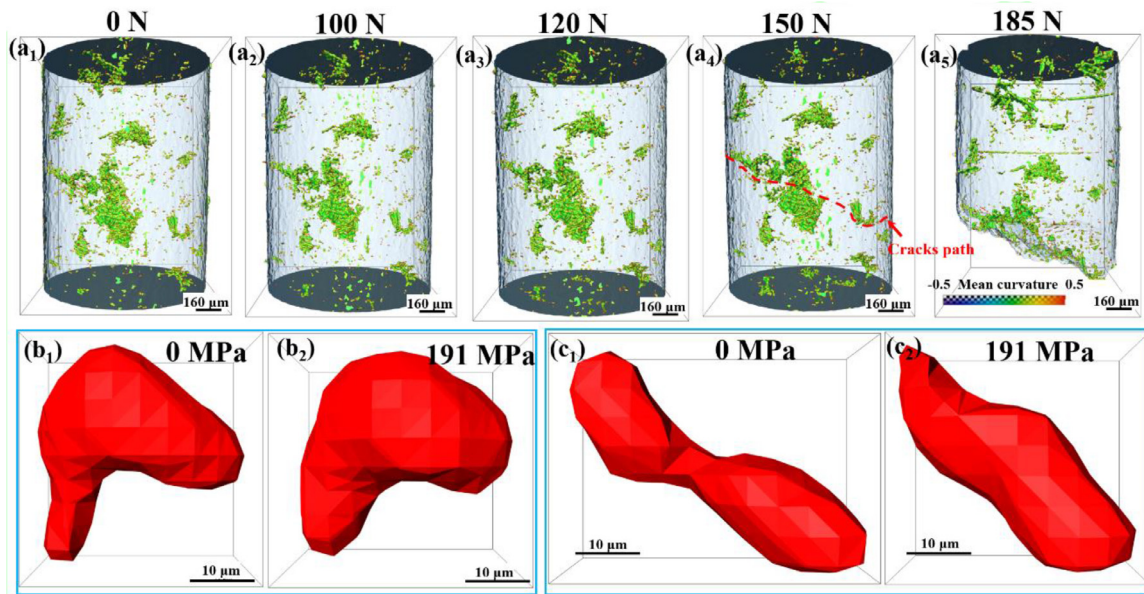

Fig. 12. *In situ* synchrotron X-ray tomography during the tensile test: (a) 3D morphology and mean curvature of pores; (b, c) the development of pores.

coarsening rate constant K can be calculated from the slope of the plot of d *versus* t. The values for 120 °C to 160 °C are 2.9×10^{-12} m$^{1.8}$/s and 3.9×10^{-11} m$^{1.5}$/s, respectively. This indicates that the diffusion rate of Cu atoms is around 13 times higher at 160 °C than that at 120 °C. This explains the difficulty to form θ' precipitates at 160 °C as it is shown by TEM and SANS results (Figs. 6 and 7). This is also in agreement with the SANS measurement. A coarsening activation energy Q of 91.9 kJ/mol has been calculated from the plot of $R\ln(K \cdot T_a)$ *versus* $1000/T_a$, Fig. 14(b). This high energy in comparison to the typical of Al-Cu binary alloys (80.2 kJ/mol) is due to the presence of Sc and Zr in the vicinity of θ' precipitates, inhibiting the diffusion of Cu atoms [16–18]. This high coarsening activation energy justifies the stability of θ' precipitates which im-

proves the mechanical resistance of the alloy. As the TEM images (Fig. 7) and alloy hardness, Fig. 5(e) and (f) shows the size of θ' precipitates at 120 °C slightly increase with ageing time. The size of θ' precipitates at the ageing temperature of 160 °C and gradually grows into a large size (about 75 nm in length at 24 h). Hence, the metastable and fine θ' evolve into large and stable θ, reducing the number of precipitates in the Al matrix that can bear the load. Hardness is almost constant at 160 °C. To obtain high mechanical properties, a two-stage ageing process and ageing time below 12 h are required at 160 °C.

In situ synchrotron X-ray diffraction was used to study the precipitation process during the ageing treatment of the 75 MPa alloy, the results are plotted in Fig. 15. The detailed process is: (i) heat-
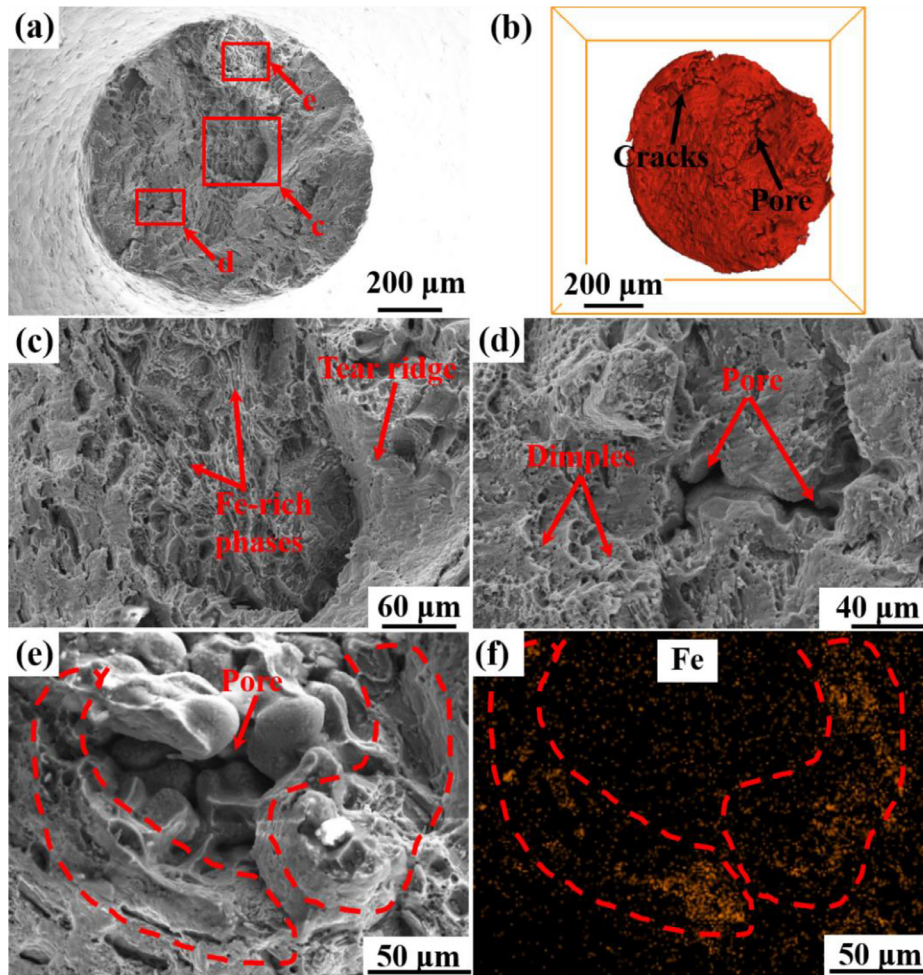
Fig. 13. Fracture surface of the *in situ* tomography studied sample: (a) SEM images; (b) 3D reconstructed fracture surface; (c–e) the enlarged SEM images of the fracture surface in (a); (f) Fe element distribution on the surface (e).
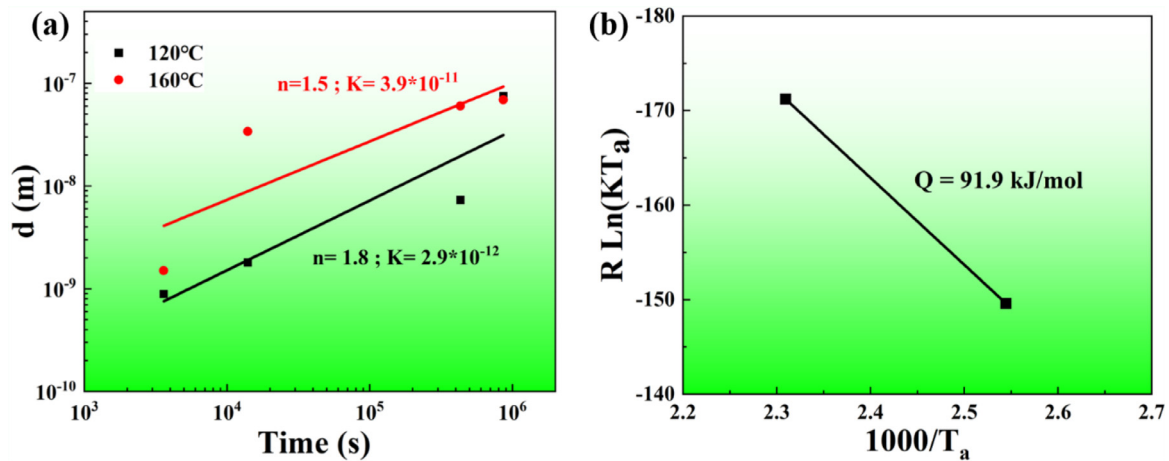

Fig. 14. Plotting of (a) *d versus t*; (b) $R\ln(K \cdot T_a)$ *vs.* $1000/T_a$ of θ' at ageing temperatures of 120 and 160 °C. *n* and *K* values obtained fitting are shown in Fig. 14(a).

ing from 28 °C to 160 °C with a constant heating rate of 5 °C/min; (ii) holding at an ageing temperature of 160 °C for 4 h. The 2D diffraction pattern, Fig. 15(a) shows the presence of α-Al and β-Fe before the ageing treatment. It is interesting to note that the patterns shift to the left side during the heating stage, while their patterns at the same 2θ location undergo a sharp decrease (or increase in some planes) in intensity when the 160 °C ageing temperature is reached. The peak shift to the left side in Fig. 15(b)–

(f) is related to the combined effect of thermal expansion of the Al crystal lattice due to the heating process [75] and the lattice emptying of Cu atoms in solid solution [76]. The intensity of Al (022), (111) patterns decrease due to the formation of θ'' and θ' precipitates. These precipitate strains and locally tilt the matrix. The tilted regions move away, (022), or approach, (111), the Bragg condition modifying the intensity of these grain families. Moreover, the supersaturated Cu atoms in the α-Al gradually precipitate dur-
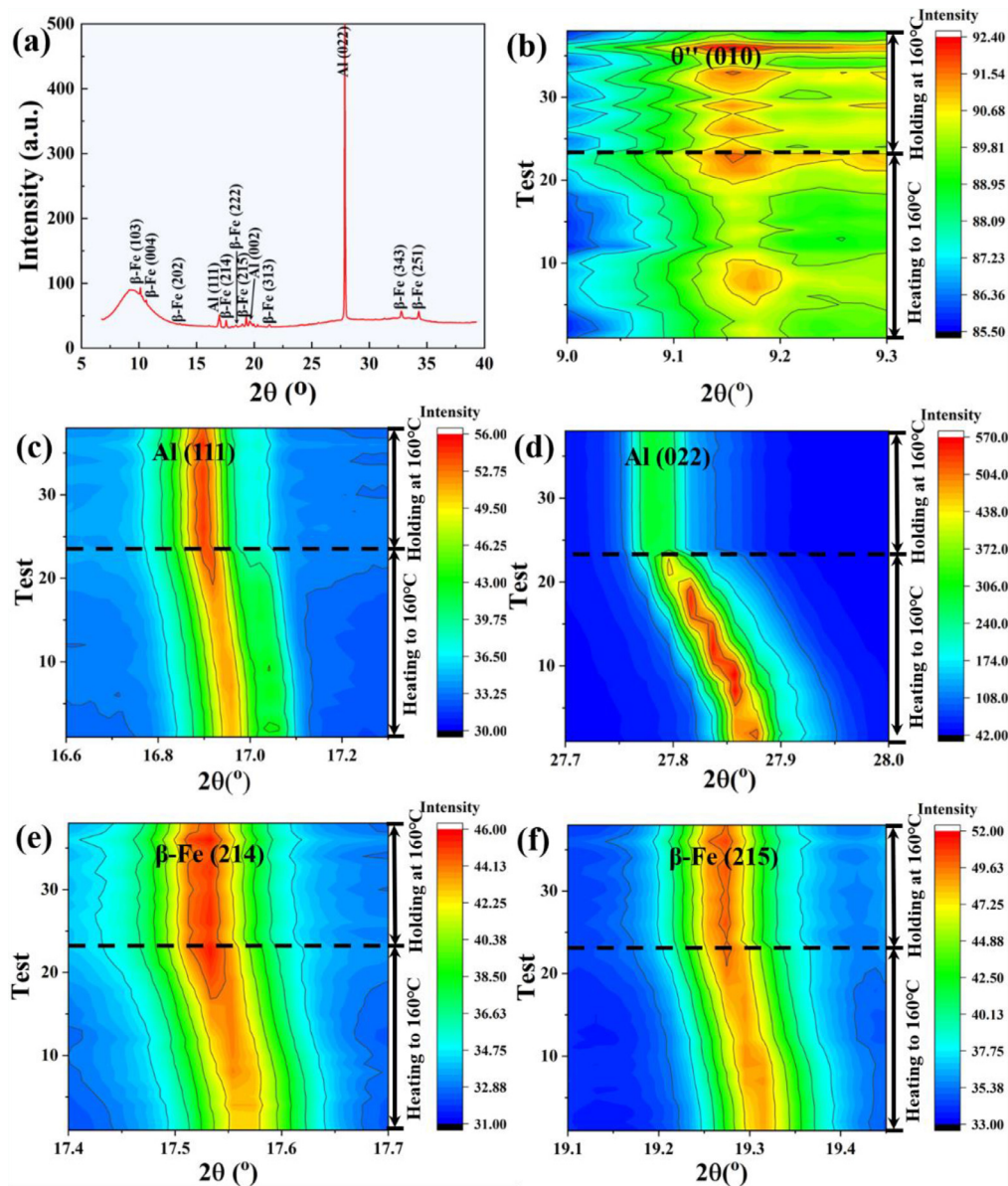
Fig. 15. *In situ* synchrotron X-ray diffraction patterns plotting of the heating and holding process at different times; (a) 1D diffraction pattern of the sample before ageing; 2D plot of θ'' (010) plane (b); Al (111) plane (c); Al (022) plane (d); β-Fe (214) plane (e); and β-Fe (215) plane (f).

ing ageing, and the θ' precipitate and α-Al have a semi-coherent orientation relationship [36]. For example, the $(001)_{\theta''}$ plane is parallel to $(001)_{Al}$. The peak of θ' precipitates can be detected by the diffraction methods [77]. Thus, the diffraction pattern of θ'' precipitates was clearly observed in the alloy during 4 h ageing (Fig. 15(b)). Also, the intensity of θ'' precipitates increases with prolong ageing time.

4.3. Mechanical behaviour

The correlation between the different phases of the alloy and the mechanical properties can be determined from the lattice strain of individual crystallographic lattice planes during tensile test using *in situ* synchrotron X-ray diffraction. Al-Cu-Mn-Fe-Sc-Zr alloy in T5 heat-treated state under 75 MPa has mechanical strength similar to that of commercial Al alloys [78–80] and shows a slightly lower mechanical strength than commercial Al alloys and similar to Al-Cu alloys modified with 0.1% Sc [19]. The main reasons explaining the modest mechanical strength of the studied al-

loy are its large grain size, Fig. 1 and the location of the necklace-shape Al$_3$(Sc, Zr) precipitates in the grain boundaries, Fig. 8. Apart from that, the influence of the high Fe content and Sc and Zr modifiers shows little effect on the size and distribution of θ'' and θ' precipitates. However, the studied alloy shows a slightly higher ductility (22.4%) than commercial, low Fe content alloys. This last aspect is especially noteworthy considering the high content of Fe-rich phases present in the alloy. The deformation of 22.4% is practically double that achieved by similar alloys, with 0.3% Fe, in the T4 state solidified in a conventional 0 MPa [68]. The ductility of Al-Cu family alloys, such as AA206, is strongly dependant on heat treatment and can be reduced by up to 2% with T7 treatment [80]. In the present case, this high ductility is achieved thanks to the combination of several microstructural features of the alloy, mainly related to the complex and slender geometry of the Fe-rich phases, Fig. 4. The geometrical complexity is shown because other β-Fe planes present a tension behaviour during the whole test, like the (214) and others are totally relaxed like the (139), Fig. 11(a). As the strain increases in the tensile test, part of the applied stress

is transferred to the β-Fe particles. As it is reported in the literature in relation to the mechanical behaviour of composite materials, the β-Fe should bear a higher load during the tensile test than the Al-matrix due to the load transference related to its high Young's modulus, around 170 GPa [81,82]. Then the load transfers from α-Al to β-Fe and results in the breakage of the Fe-rich interphase with the aluminium matrix because of the high local stress generated during the tensile test. The fracture of the β-Fe interphase saturates around 8% of strain, Fig. 11(a). This breakage phenomenon was observed in our previous study [47] and it corresponds to a flat or negative evolution of the FWHM of the β-Fe phase during the tensile test (Fig. 11(b)). In the Al matrix a decrease of the FWHM is also observed up to 8% strain, Fig. 11(b) associated to the relaxation process produced by such breakage of the Fe-rich/Al matrix interface. Despite this β-Fe and interphase failure, the matrix hardening associated to the interaction amongst dislocations and with precipitates provides a net hardening in the stress-strain curve (Fig. 11(c)). This hardening is also reflected with an increase in the FWHM of the matrix from 8% (Fig. 11(c)).

The Al matrix of the Al-Cu-Mn-Fe-Sc-Zr alloy shows a linear evolution of the lattice strain up to values considerably higher than yield stress (Fig 11(a)). In (220) grains this behaviour is maintained up to 8% engineering strain and in (111) grains up to 12%. The existence of the linear behaviour up to such high strain values contrasts with that usually found in other aluminium alloys with the presence of second phases [58]. Moreover, in the (200) and (220) grain families the micro-strain (type III) saturates around 12%. However, in the (111) grains the strain (type III) grows continuously up to 17% (exceeding its lattice strain at (220)) and starts to fall. Therefore, the (111) grains reach a higher microstrain which is associated with a denser dislocation structure. This behaviour has been previously found in aluminium alloys deformed at high temperatures [83]. The α-Al starts to yield and the strain accumulates during the tensile test and the proliferation and annihilation of dislocations happen at the same time. However, the lattice strains of β-Fe remain stable. This may be because the brittle β-Fe particles are already fragmented at 6% engineering strain. Finally, at stage 3, the dislocation proliferation is smaller than the dislocation annihilation. when the engineering strains are $\varepsilon > 20.5\%$, the lattice strain of α-Al and β-Fe suddenly drops to nearly zero. As shown in the *in situ* tomography results (Fig. 11), the large volume fraction of interconnected shrinkage pores dominates the 0 MPa sample breakage. In the 75 MPa sample, the Fe-rich particles dominate the fracture sample. In the present case, their complex shape distributes the damage very homogeneously across the sample explaining its high ductility, Fig. 11(g).

5. Conclusions

In the present study, the solidification, precipitation, and deformation behaviour in Al-Cu-Mn-Fe-Sc-Zr alloys were comprehensively studied by SEM, DSC, XRD, TEM, nanoindentation, nano-scale and micro-scale SRXCT, SANS, and *in situ* SRXD methods. The main results are summarized as follows:

(1) The applied pressure during solidification is helpful to refine the size of Chinese-script α(MnFe)and plate-like β-Fe phases. Pores are eliminated by 75 MPa applied pressure during the solidification of the alloy.
(2) The Fe-rich phases in the as-cast state present a complex 3D morphology of interconnected structures. The interconnectivity is greatly reduced after T5 heat treatment. The spherical bumps and holes in the interdendritic region have been visualized by high-resolution SRXCT.
(3) The size of θ' precipitates increases with increasing ageing time and temperature, while the size of T and $Al_3(ScZr)$ phases are

relatively stable. The precipitates coarsening activation energy of 91.9 kJ/mol is due to the presence of Sc and Zr in the alloy. Precipitates diffraction peaks shift to the left side due to the thermal expansion of the Al crystal lattice during heating and the reduction of supersaturated Cu atoms in the α-Al due to the formation of the coherent θ' precipitate in α-Al.
(4) At stage 1 (below 8% engineering strain), the lattice strain linearly increases both for β-Fe and aluminium matrix. At stage 2, the lattice strain remains stable with increasing engineering strain in β-Fe (222) and β-Fe (004); while slightly decreases in β-Fe (214) and β-Fe (103) plane. The elastic modulus mismatch between α-Al and β-Fe is the main reason for the stress concentration and the β-Fe fracture.
(5) The complex shape and the loss of interconnectivity of the Ferich particles due to the T5 heat treatment homogenize the damage accumulation. This explains the high ductility of the modified Al-Cu alloy despite its high Fe content.

Acknowledgements

Supplementary materials

Supplementary material associated with this article can be found, in the online version, at doi:10.1016/j.jmst.2023.03.008.

References

[1] T.H. Muster, A.E. Hughes, G.E. Thompson, Copper Distribution in Aluminium Alloys, Nova Science Publishers, New York, 2009.
[2] M. Schöbel, R. Fernández, R. Koos, J. Bernardi, J. Alloy. Compd. 775 (2019) 617–627.
[3] S. Bahl, X. Hu, E. Hoar, J. Cheng, J.A. Haynes, A. Shyam, Mater. Sci. Eng. A 772 (2020) 138801.
[4] Y.L. Zhao, W.X. He, D.F. Song, F.H. Shen, X.X. Li, Z.Z. Sun, Y. Wang, S.H. Liu, Y. Du, R. Fernández, Ultrason. Sonochem. 89 (2022) 106139.
[5] Y.L. Zhao, D.F. Song, H.L. Wang, X.X. Li, L.J. Chen, Z.Z. Sun, Z. Wang, T.G. Zhai, Y.N. Fu, Y. Wang, S.H. Liu, Y. Du, W.W. Zhang, Intermetallics 146 (2022) 107584.
[6] D.F. Song, Y.L. Zhao, Y.W. Jia, R.X. Li, N. Zhou, K.H. Zheng, Y.N. Fu, W.W. Zhang, J. Alloy. Compd. 915 (2022) 165378.
[7] W.W. Zhang, B. Lin, Z. Luo, Y.L. Zhao, Y.Y. Li, J. Mater. Res. 30 (2015) 2474–2484.
[8] B. Lin, W. Zhang, X. Zheng, Y. Zhao, Z. Lou, W. Zhang, Mater. Charact. 150 (2019) 128–137.
[9] Y.L. Zhao, B. Lin, D.F. Song, D.H. Zheng, Z.Z. Sun, C.X. Xie, W.W. Zhang, Materials 12 (2019) 3904.
[10] W.W. Zhang, Y.L. Zhao, D.T. Zhang, Z.Q. Luo, C. Yang, Y.Y. Li, Trans. Nonferr. Met. Soc. 28 (2018) 1061–1072.
[11] J.Y. Zhang, Y.H. Gao, C. Yang, P. Zhang, J. Kuang, G. Liu, J. Sun, Rare Met. 39 (6) (2020) 636–650.
[12] C. Yang, L.F. Cao, Y.H. Gao, P.M. Cheng, P. Zhang, J. Kuang, J.Y. Zhang, G. Liu, J. Sun, Mater. Des. 186 (2020) 108309.
[13] M.R. Ghomashchi, A. Vikhrov, J. Mater. Process. Technol. 101 (2000) 1–9.
[14] K. Hu, C. Lin, S. Xia, C. Zheng, B. Lin, Mater. Charact. 170 (2020) 110680.
[15] B. Zhao, S. Xing, A. Shan, G. Yan, X. Jiang, Intermetallics 153 (2023) 107783.
[16] Y.L. Zhao, W.W. Zhang, C. Yang, D.T. Zhang, Z. wang, J. Mater. Res. 33 (2018) 898–911.
[17] Q.L. Li, Y.S. Zhang, Y.F. Lan, Y.X. Zhang, T.D. Xia, J. Alloy. Compd. 831 (2020) 154739.
[18] Y.H. Gao, L.F. Cao, C. Yang, J.Y. Zhang, G. Liu, J. Sun, Mater. Today Nano 6 (2019) 100035.

[19] Y.H. Gao, L.F. Cao, J. Kuang, J.Y. Zhang, G. Liu, J. Sun, J. Mater. Sci. Technol. 37 (2020) 38–45.
[20] S. Bai, X. Yi, G. Liu, Z. Liu, J. Wang, J. Zhao, Mater. Sci. Eng. A 756 (2019) 258–267.
[21] Y.H. Gao, L.F. Cao, J. Kuang, H. Song, G. Liu, J.Y. Zhang, J. Sun, Mater. Sci. Eng. A 803 (2021) 140509.
[22] Y. Li, B. Hu, B. Liu, A.M. Nie, Q.F. Gu, J.F. Wang, Q. Li, Acta Mater. 187 (2020) 51–65.
[23] Y. Li, Y. Jiang, B. Liu, Q. Luo, B. Hu, Q. Li, J. Mater. Sci. Technol. 65 (2021) 190–201.
[24] J. Xu, Y. Li, K. Ma, Y.N. Fu, E.Y. Guo, Z.N. Chen, Q.F. Gu, Y.X. Han, T.M. Wang, Q. Li, Scr. Mater. 187 (2020) 142–147.
[25] Q. Luo, X. Li, Q. Li, L. Yuan, L. Peng, F. Pan, W. Ding, J. Mater. Sci. Technol. 135 (2023) 97–110.
[26] J. Xu, Y. Li, B. Hu, Y. Jiang, Q. Li, J. Mater. Sci. 54 (2019) 14561–14576.
[27] Y. Li, Y. Jiang, B. Hu, Q. Li, Scr. Mater. 187 (2020) 262–267.
[28] Y. Li, B. Hu, Q. Gu, B. Liu, Q. Li, Scr. Mater. 160 (2019) 75–80.
[29] Y.P. Pang, D.K. Sun, Q.F. Gu, K.C. Chou, X.L. Wang, Q. Li, Cryst. Growth Des. 16 (2016) 2404–2415.
[30] Q. Luo, J.D. Li, B. Li, B. Liu, H.Y. Shao, Q. Li, J. Magnes. Alloy. 7 (2019) 58–71.
[31] Q. Luo, Y.L. Guo, B. Liu, Y.J. Feng, J.Y. Zhang, Q. Li, K.C. Chou, J. Mater. Sci. Technol. 44 (2020) 171–190.
[32] S.M. Amer, R.Y. Barkov, A.S. Prosviryakov, A.V. Pozdniakov, Phys. Met. Metall. 122 (2021) 915–922.
[33] O.I. Mamzurina, S.M. Amer, I.S. Loginova, M.V. Glavatskikh, A.G. Mochugovskiy, R.Y. Barkov, A.V. Pozdniakov, Metals 12 (2022) 479.
[34] S.K. Kairy, B. Rouxel, J. Dumbre, J. Lamb, T.J. Langan, T. Dorin, N. Birbilis, Corros. Sci. 158 (2019) 108095.
[35] J. Qin, P. Tan, X. Quan, Z. Liu, D. Yi, B. Wang, J. Alloy. Compd. 909 (2022) 164686.
[36] L. Jiang, B. Rouxel, T. Langan, T. Dorin, Acta Mater. 206 (2021) 116634.
[37] L. Jiang, T. Langan, T. Wood, P. Sanders, T. Dorin, Scr. Mater. 210 (2022) 114452.
[38] J.U. Rakhmonov, S. Bahl, A. Shyam, D.C. Dunand, Acta Mater. 228 (2022) 117788.
[39] R. Santos-Güemes, B. Bellón, G. Esteban-Manzanares, J. Segurado, L. Capolungo, J. LLorca, Acta Mater. 188 (2020) 475–485.
[40] C.M. Jeffries, J. Ilavsky, A. Martel, S. Hinrichs, A. Meyer, J.S. Pedersen, A.V. Sokolova, D.I. Svergun, Nat. Rev. Methods Primers 1 (2021) 70.
[41] A. Deschamps, F.D. Geuser, J. Appl. Cryst. 44 (2011) 343–352.
[42] V.D. Sitdikov, M. Yu Murashkin, R.Z. Valiev, J. Alloy. Compd. 735 (2018) 1792–1798.
[43] E.W. Huang, C.S. Tsao, M.H. Wen, T.Y. Kuo, S.Y. Tu, B.W. Wu, C.J. Su, U.S. Jeng, J. Mater. Res. 29 (2014) 874–879.
[44] P.J. Withers, C. Bouman, S. Carmignato, V. Cnudde, D. Grimaldi, C.K. Hagen, E. Maire, M. Manley, A.D. Plessis, S.R. Stock, Nat. Rev. Methods Primers 1 (2021) 18.
[45] Y.L. Zhao, W.W. Zhang, D.F. Song, B. Lin, F.H. Shen, D.H. Zheng, C.X. Xie, Z.Z. Sun, Y.N. Fu, R.X. Li, J. Mater. Sci. Technol. 80 (2021) 84–99.
[46] Y. Zhao, W. Du, B. Koe, T. Connolley, S. Irvine, P.K. Allan, C.M. Schlepütz, W. Zhang, F. Wang, D.G. Eskin, J. Mi, Scr. Mater. 146 (2018) 321–326.
[47] Y.L. Zhao, Z. Wang, C. Zhang, W.W. Zhang, J. Alloy. Compd. 777 (2019) 1054–1065.
[48] Y.L. Zhao, D.F. Song, B. Lin, C. Zhang, D.H. Zheng, S. Inguva, T. Li, Z.Z. Sun, Z. Wang, W.W. Zhang, Mater. Charact. 153 (2019) 354–365.
[49] C.S. Kaira, T.J. Stannard, V.D. Andrade, F.D. Carlo, N. Chawla, Acta Mater. 176 (2019) 242–249.
[50] Z. Li, N. Limodin, A. Tandjaoui, P. Quaegebeur, J. Witz, D. Balloy, Mater. Sci. Eng. A 794 (2020) 139920.
[51] H. Su, T. Yoshimra, H. Toda, M.S. Bhuiyan, K. Uesugi, A. Takeuchi, N. Sakaguchi, Y. Watanabe, Metall. Mater. Trans. A 47 (2016) 6077–6089.
[52] L. Wang, N. Limodin, A. ElBartali, J. Witz, R. Seghir, J. Buffiere, E. Charkaluk, Mater. Sci. Eng. A 673 (2016) 362–372.
[53] L. Wang, N. Limodin, A. ElBartali, J. Witz, J. Buffiere, E. Charkaluk, Metall. Mater. Trans. A 51 (2020) 3843–3857.
[54] W. Qian, S. Wu, Z. Wu, Ahmed S, W. Zhang, G. Qian, P.J. Withers, Int. J. Fatigue (2022) 106616.
[55] J. Bao, S. Wu, P.J. Withers, Z. Wu, F. Li, Y. Fu, W. Sun, Mater. Sci. Eng. A 792 (2020) 139809.
[56] Z.Y. Wang, S.C. Wu, G.Z. Kang, H. Li, Z.K. Wu, Y.N. Fu, P.J. Withers, Acta Mater. 211 (2021) 116881.
[57] S.C. Wu, T.Q. Xiao, P.J. Withers, Eng. Fract. Mech. 182 (2017) 127–156.
[58] M. Wang, M. Knezevic, H. Gao, J. Wang, M. Kang, B. Sun, Mater. Charact. 179 (2021) 111322.
[59] M. Wang, Y. Zhou, H. Lv, M. Li, H. Gao, J. Wang, B. Sun, J. Alloy. Compd. 882 (2021) 160692.
[60] G. Garcés, A. Orozco-Caballero, J.Q. Fonseca, P. Pérez, J. Medina, A. Starkd, N. Schelle, P. Adeva, Mater. Sci. Eng. A 772 (2020) 138716.
[61] N.B. Zhang, S.H. Guo, X.H. Gong, Y.Y. Zhang, S. Chen, B.B. Zhang, L. Lu, X.H. Yao, Mater. Charact. 179 (2021) 111349.
[62] D. Zhang, L. Wang, H. Zhang, A. Maldar, G. Zhu, W. Chen, J. Park, J. Wang, X. Zeng, Acta Mater. 189 (2020) 93–104.
[63] Y.L. Zhao, D.F. Song, H.L. Wang, Y.W. Jia, B. Lin, Y. Tang, Y. Tang, D. Shu, Z.Z. Sun, Y.N. Fu, W.W. Zhang, J. Alloy. Compd. 901 (2022) 163666.
[64] R.C. Chen, D. Dreossi, L. Mancini, R. Menk, L. Rigon, T.Q. Xiao, R. Longo, J. Synchrotron Radiat. 19 (2012) 836–845.
[65] Q. Yuan, K. Zhang, Y. Hong, W. Huang, K. Gao, Z. Wang, P. Zhu, J. Gelb, A. Tkachuk, B. Hornberger, M. Feser, W. Yun, Z. Wu, J. Synchrotron Rad. 19 (2012) 1021–1028.
[66] Y.B. Ke, C.Y. He, H.B. Zheng, Y.S. Geng, J.Y. Fu, S.K. Zhang, H.T. Hu, S.L. Wang, B. Zhou, F.W. Wang, J.Z. Tao, Neutron News 29 (2018) 14.
[67] S.R. Kline, J. Appl. Crystallogr. 39 (2006) 895–900.
[68] X. Wu, B. Wang, C. Rehm, H. He, M. Naeem, S. Lan, Z. Wu, X. Wang, Acta Mater. 222 (2022) 117446.
[69] Y.H. Gao, J. Kuang, G. Liu, J. Sun, Mater. Sci. Eng. A 746 (2019) 11–26.
[70] R. Fernández, G. Bokuchava, Giovanni, I. Serrano-Muñoz, G. González-Doncel, J. Appl. Crystallogr. (2023) Under revision.
[71] X. Luo, H. Fang, H. Liu, Y. Yan, H. Zhu, K. Yu, Mater. Trans. 60 (2019) 737–742.
[72] Z. Chen, Y. Zhao, Z. Zhang, Vacuum 189 (2021) 110263.
[73] I.M. Lifshitz, V.V.J. Slyozov, J. Phys. Chem. Solids 19 (1961) 35–50.
[74] T. Naseri, D. Larouche, P. Heugue, R. Martinez, F. Breton, D. Massinon, Philos. Mag. 101 (2021) 1–24.
[75] H. Fröck, C. Rowolt, B. Milkereit, M. Reich, W. Kowalski, A. Stark, O. Kessler, J. Mater. Sci. 56 (2021) 19697–19708.
[76] R. Fernández, G. Bokuchava, I. Toda-Caraballo, G. Bruno, V. Turchenko, Y. Gorshkova, G. González- Doncel, Adv. Eng. Mater. 22 (2020) 1901355.
[77] B. Milligan, D. Ma, L. Allard, A. Clarke, A. Shyam, Acta Mater. 205 (2021) 116577.
[78] M. Schwankl, J. Wedler, C. Körner, J. Mater. Process. Technol. 238 (2016) 160–168.
[79] K. Liu, X. Cao, X.G. Chen, Metall. Mater. Trans. A 45 (2014) 2498–2507.
[80] K. Liu, X. Cao, A. Bolouri, X.G. Chen, M. Tiryakioğlu, W. Griffiths, M. Jolly, Shape Casting, The Minerals, Metals & Materials Series, Springer, Cham, 2019.
[81] J. Tian, Y. Zhao, Z. Wen, H. Hou, P. Han, Solid State Commun. 257 (2017) 6–10.
[82] F. Tang, T. Gnäupel-Herold, H. Prask, I. Anderson, Mater. Sci. Eng. A 399 (2005) 99–106.
[83] I. Serrano-Munoz, R. Fernández, R. Saliwan-Neumann, G. González-Doncel, G. Bruno, J. Appl. Crystallogr. 55 (2022) 860–869.